Nematic liquid crystals on spherical surfaces: Control of defect configurations by temperature, density, and rod shape

Subas Dhakal, Francisco J. Solis, and Monica Olvera de la Cruz

Phys. Rev. E **86**, 011709 — Published 23 July 2012

DOI: 10.1103/PhysRevE.86.011709

Nematics on spherical surfaces: Control of defect configurations by temperature, density, and rod shape.

Subas Dhakal,[1] Francisco J. Solis,[2] and Monica Olvera de la Cruz[1,*]

[1]*Department of Materials Science, Northwestern University, Evanston, Illinois 60208*
[2]*Division of Mathematical and Natural Sciences, Arizona State University, Glendale, Arizona 85306*

(Dated: May 30, 2012)

Recent experiments have shown that defect conformations in spherical nematics can be controlled through variations of temperature, shell thickness, and other environmental parameters. These modifications can be understood as a result of the induced changes in the effective elastic constants of the system. To characterize the relation between defect conformations and elastic anisotropy we carry out Monte Carlo simulations of a nematic on a spherical surface. As the anisotropy is increased the defects flow from a tetrahedral arrangement to two coalescing pairs and then to a great circle configuration. We also analyze this flow using a variational method based on harmonic configurations.

PACS numbers: 61.30.Dk, 61.30.Cz, 64.70.mf

I. INTRODUCTION

Liquid crystals confined to curved geometries exhibit, quite generally, topological defects [1]. These structures are of current interest because of their prospective use as building blocks for meso-structures [2]. Topological defects on these surfaces organize in robust but controllable patterns. The defect sites at the surface of colloids or nano-particles can be functionalized to dictate the organization of multi-particle aggregates. Such large-scale organization of functionalized nano-particles has already been achieved [3]. Investigations of defect arrangements in spherical nematics create an avenue for the discovery of new self-assembling structures. The purpose of this work is to offer new insight into the defect structure in these systems, focusing on spherical geometries. We carry out simulations that map the flow of defects as environmental conditions are changed, and we provide heuristic insight into this behavior using a variational method.

We can understand the defect structure as determined by changes in the effective elastic constants of the nematic. These constants are in turn controlled by microscopic and environmental parameters. In two-dimensional objects, the nematic field can be effectively described by the Frank free energy, a mean-field theory for the local director of the field that uses just two elastic parameters: the splay K_{11} and bend K_{33} elastic moduli. The free energy of this field theory is

$$F = \frac{1}{2}\int \sqrt{g}[K_{11}(\vec{D}\cdot\vec{\boldsymbol{n}})^2 + K_{33}(\vec{\boldsymbol{n}}\times\vec{D}\times\vec{\boldsymbol{n}})^2]d^2x, \quad (1)$$

where $\vec{\boldsymbol{n}}$ is the nematic director describing the local molecular orientation, $\sqrt{g}$ is metric of the surface, and the operator $\vec{D}$ is the covariant derivative on the surface of the sphere. A central goal of our simulations and analytical investigations is to map the dependence of the elastic constants of the system on microscopic and environmental details.

A number of theoretical studies [1, 2, 4] have investigated in detail the director field and defect positions for $K_{11} = K_{33}$ (the one-constant approximation). It has been clearly shown that, in this approximation, the minimum energy configurations of a spherical nematic comprise four $+1/2$ point defects at the vertices of a tetrahedron inscribed in the sphere. It is also known, however, that differences in the effective values of the elastic constants are enhanced in finite systems.

Several theoretical and computational approaches have been used to investigate the interaction between the surface curvature and the topological defects of the texture [5–13]. Despite these studies, many features of the defect configurations, even in the simple geometry of a sphere, are not known. Experimentally, on the other hand, a novel type of double emulsions of nematic liquid crystals has been developed that allows the study of defect structures in thin nematic shells [14–17]. These structures range from $30 - 100\mu m$ in size and are quite stable when the line-interfacial energy is too large to allow deformations. In a series of recent experiments [14–17], it has been shown that the bend elastic constant of a spherical nematic diverges near the transition to the SmA phase, and a continuous evolution of the defect structure from a tetrahedral to a great circle configuration has been revealed upon lowering the temperature. These experiments lead to an important question regarding the mechanism governing the defect evolution and how it changes with the microscopic parameters.

Although earlier simulations [5–7] focused on the effects of unequal elastic constants, there are still a number of open questions. First, a quantitative test of the defect evolution in a thin nematic shell for the whole range of elastic anisotropy has not been carried out thus far; we are able in the present work to simulate a sys-

*Electronic address: m-olvera@northwestern.edu

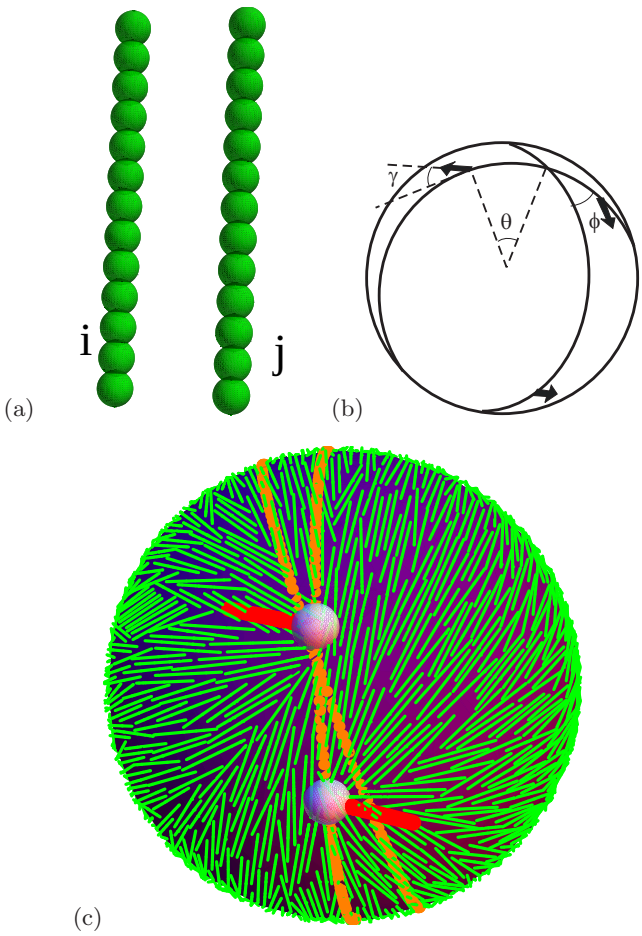

FIG. 1: (Color online) (a) Nematic molecules are represented as rods made up of connected spheres. The interaction between the rods is modeled as the sum of the interactions between beads. (b) Scheme to describe the defect structure in spherical nematic. The defect positions and orientation are defined by three angles θ, ϕ, and γ. (c) Simulation configuration at a very high density. The defects in each pair on either hemisphere are close to each other.

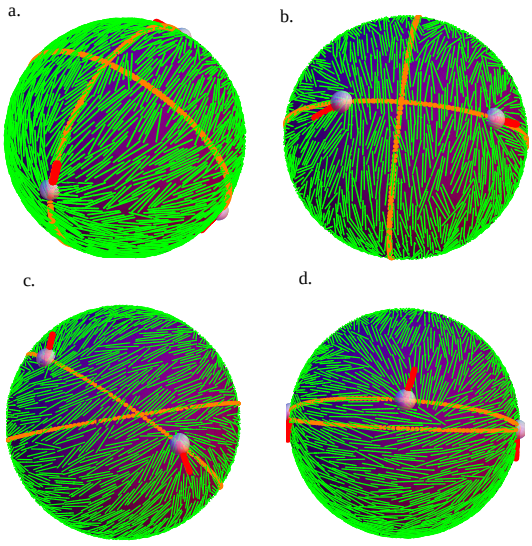

FIG. 2: (Color online) Evolution with temperature of defect configurations in a spherical nematic. Results correspond to simulations at $u/k_BT = 1.37, 2.22, 4.0$ and 40.0 (a, b, c and d). The small spheres represent a defect location, and defect orientations are shown as red-vectors. As temperature is lowered in the nematic phase, there is a continuous transition from a high-temperature tetrahedral configuration characterized by $\epsilon \approx 0$ to a low-temperature great circle configuration with much stronger elastic anisotropy $\epsilon \approx 1$. We pair nearest-neighbor defects and associate a great circle to each of the pairs. At high temperatures we observe a tetrahedral arrangement with the angle between great circles $\approx \pi/2$. The angle continuously decreases with temperature and at very low temperatures the great circles coincide and the defect directors are perpendicular to them.

tem over a wide range of elastic anisotropy by employing the new simulation model. The role of the microscopic parameters is also of importance: rod lengths, density, droplet size, etc., influence the defect configuration on the sphere. We quantitatively connect these values to the effective Frank constants that describe the textures. Another novel aspect of our work is the exploitation of symmetries of the ground state of the system at different anisotropy values: we introduce a useful set of coordinates for the overall structure of the defects. Finally, we also introduce a variational approach to the study of textures in curved geometries that complements other analytical approaches to the problem.

We investigate the problem with two different methods. First, we carry out a series of Monte Carlo simulations over a wide range of parameters leading to inferred values of elastic anisotropy in the range $0 \leq \epsilon \leq 0.9$, where ϵ is defined as the normalized ratio of the difference between splay and bend elastic constants, i.e., $\epsilon = (K_{33} - K_{11})/(K_{33} + K_{11})$. Then, we analyze the defect flow using a variational approach and show that the results of these approaches are consistent, especially in the low-anisotropy range. The picture that emerges from these approaches provides a better understanding of the ways in which external factors control the defect location transformation.

This paper is organized as follows. In Sec.II we discuss the simulation model. We describe a technique to estimate the inferred value of the elastic anisotropy in simulations with a planar approximation in Sec.III. In Sec.IV, we give the results of Monte Carlo simulations and provide the quantities measured in the simulations. We discuss the variational approach in Sec.V. Finally, in Sec.VI, we discuss and summarize the conclusions of this study. Appendix A presents some technical details associated with the variational calculation.

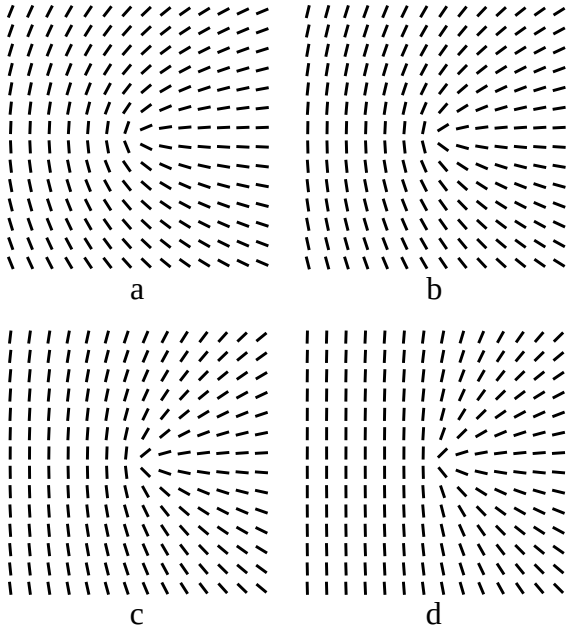

FIG. 3: Asymptotic nematic textures on a plane around a defect core for different values of elastic anisotropy: (a) $\epsilon = 0.0$,(b) $\epsilon = 0.30$, (c) $\epsilon = 0.60$, and (d) $\epsilon = 0.90$. These textures have angular but not radial dependence.

II. SIMULATION MODEL

We simulate the nematic as rods formed by connected spherical beads with each bead representing an interaction site as shown in Fig. 1. This method has been widely used in simulations of the liquid-crystalline phase behavior in different systems [18–20]. In this approach, the rods are assumed to be perfectly rigid, i.e., the intra-bead interaction is ignored. As the goal in these simulations is to explore the defect structure in the nematic phase, only the excluded volume interaction between rods is necessary to recover the phase behavior of interest. The interaction between the component beads is described via the Weeks-Chandler-Anderson potential [21]:

$$U_{ij}^{\alpha\beta} = \begin{cases} 4u\left[\left(\frac{\sigma}{r_{ij}}\right)^{12} - \left(\frac{\sigma}{r_{ij}}\right)^{6}\right] + u, & if\ r_{ij} \leq 2^{1/6}\sigma \\ 0, & otherwise, \end{cases} \tag{2}$$

where $r_{ij} = |\vec{r}_i - \vec{r}_j|$ and i and j are the beads indices on different molecules α and β. Here, σ defines the hard-core diameter of a single bead. In this model, the elastic anisotropy of in-plane nematic order is controlled by rod length (l), overall density (ρ), interaction strength (u/k_BT) and sphere radius (R). In our simulations, the length and energy scales are defined by σ and u, respectively. In this paper, we use $\sigma = 1.0$ and $u = 4.0$ unless otherwise specified.

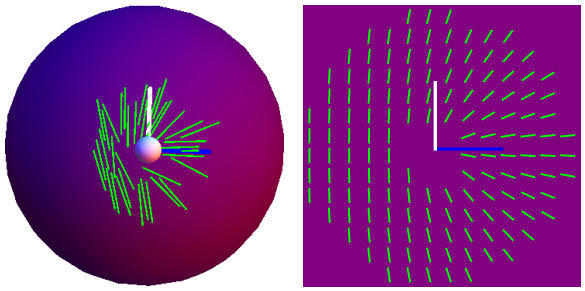

FIG. 4: (Color online) Comparisons of nematic textures around a defect core: On a sphere around a $+1/2$ defect (snapshot from simulations) and on the plane with an enforced boundary condition to have a $+1/2$ defect at the center for $\epsilon = 0.74$. We match the texture on the sphere with that of the plane to estimate the elastic anisotropy in our simulations.

III. ESTIMATION OF ELASTIC ANISOTROPY IN SIMULATIONS

In a system constrained on a spherical surface, the observed textures are the result of local and global factors. In close proximity to a point defect, the local texture is determined by the values of the effective coupling constants while, at longer scales, the texture will also depend on the interaction between the fields associated with each defect [23]. We exploit this idea to extract the effective coupling constant ϵ from our simulation results. We compare the nematic texture on the sphere around a defect core to the asymptotic plane solution obtained when the radial dependence of the texture is ignored [24]. It can be shown that the asymptotic solution in the plane is also the asymptotic solution on a sphere. We position a $+1/2$ defect at the center of a flat system of coordinates as shown in Fig. 4(b) and write a nematic field of the form $\hat{\boldsymbol{n}} = (\cos(\psi+\phi), \sin(\psi+\phi))$, where ψ measures the orientation of the field with respect to the radial vector. It can be shown that the free energy density reduces to $f = (1+\epsilon\cos 2\psi)(1+\psi')^2/2r$, where the prime indicates the derivative with respect to the two-dimensional polar angle ϕ. The equation that describes the free energy minimum can be integrated to obtain a first-order relation for $\psi(\phi)$:

$$\frac{d\psi}{d\phi} = \sqrt{\frac{1-\epsilon\cos 2\psi}{p-\epsilon\cos 2\psi}} \tag{3}$$

where p is an integration constant that is set by the strength of the defect and the anisotropy parameter ϵ. This last equation can also be explicitly integrated, and $p(\epsilon)$ can be determined as a solution to a transcendental equation. We use these expressions to estimate the value of ϵ for a given director pattern around a defect; some examples are shown in Fig. 3. In each simulation, we set a planar reference frame with an axis aligned with the defects directors. The orientation of the rods in a

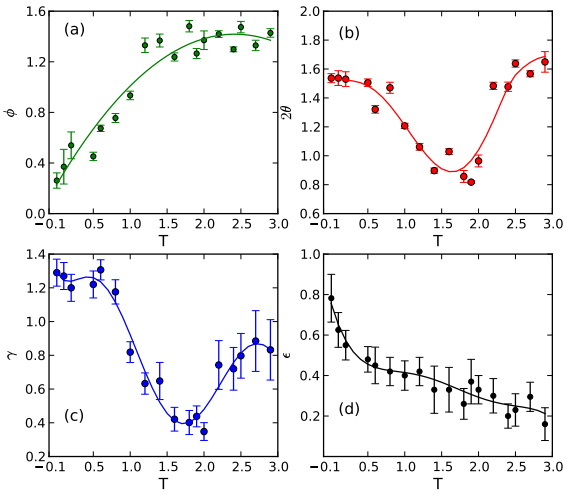

FIG. 5: (Color online) Monte Carlo simulation results: (a-c) Different angles as functions of temperature for a system of $N = 1600, l = 15\sigma$ at a fixed surface density($\rho \approx 0.42$). The final droplet size is 59.99σ in LJ units. (d) Elastic anisotropy as functions of temperature. The solid lines are merely guides to the eye.

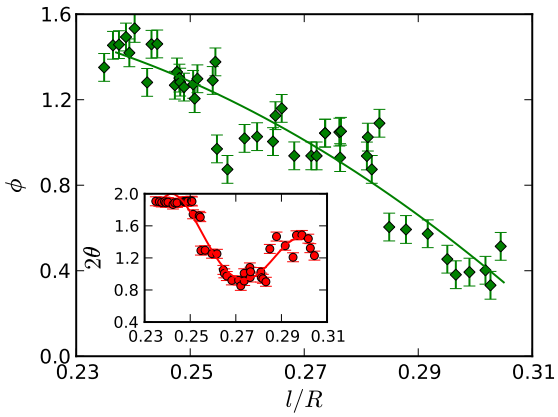

FIG. 6: (Color online) Variation of θ and ϕ as a function of l/R at $u/k_BT = 1.33$. The great circle angle (ϕ) decreases smoothly with density (l/R). However, the distance between the pair of defects (θ) on each hemisphere initially decreases and finally increases with l/R. In these simulations, we consider three different rod lengths $l = 13\sigma, 15\sigma$ and 17σ. The corresponding droplet sizes range from $52.96\sigma - 63.85\sigma$ in LJ units. The solid lines are simply guides to the eye.

neighborhood of the defect gives a set of pairs (ϕ, ψ). An approximate value of ϵ is then extracted by a least-square comparison between these pairs and the values of $\psi(\phi)$ at the same location for different values of ϵ. The inferred values of ϵ are averaged over both time and four defects of each configuration.

The determination of the defect position involves, in addition to the statistical fluctuations associated with the simulation method, further uncertainties due to the finite sizes of the rods. In a given configuration, the order-parameter, the position and orientation of a defect core is determined using a finite set of neighboring rods. The neighborhood considered has a radius 1.5 l. Our results retain some dependence on the size of the region used, and this procedure introduces further uncertainties in the determination of other derived quantities. We have checked, however, that the results are not highly sensitive to the specific size of the region. Our plots show error estimates that arise from both statistical fluctuations and other systematic errors.

IV. MONTE CARLO SIMULATION

We have carried out constant - *NPT* Monte Carlo simulations of rod-like molecules on a spherical surface interacting via the potential in Eq. (2). In all of these simulations, we enforce a planar anchoring for the orientation of the rods. Each Monte Carlo cycle consists of random translations and reorientations of all N rods and a compression move. The moves are accepted or rejected in accordance with the standard Metropolis algorithm. The translation and reorientation move is accepted with transition probability $P_{acc} = min(1, exp(-(E_f - E_i))$. For the compression move, the area of the spherical shell is allowed to fluctuate, and we replace the energy of each microstate by the enthalpy $H(i) = E(i) + \sigma A(i)$, where σ is the surface tension. So the transition probability, in the Metropolis scheme, for this move is $P_{acc} = min(1, exp(-\Delta H))$, where; $\Delta H = (E_f - E_i) + (A_f - A_i)$, A_f = final area, and A_i = initial area. We monitor the energy of the system to ensure that equilibrium is reached. A typical run consists of $\sim 10^7$ Monte Carlo steps for each σ. The system is compressed slowly with increasing σ in steps of 0.01, or 0.001 at very low temperatures and high densities.

To investigate the effect of temperature on the defect structure we simulated a system of $N = 1600$ rods ($l = 15\sigma$) at different temperatures. We start with a random state and gradually compress the system until the desired density of $\rho \approx 0.42$ is reached. Here the surface density is defined as $\rho = NN_b\pi\sigma^2/(16\pi R^2)$, where N_b is the number of beads on each rod. Figures 2(a-d) show nematic textures obtained in these simulations. To identify the defect locations, we calculate the local nematic order parameter, which is the largest eigen-value of the nematic order tensor $Q_{\alpha\beta}(\vec{r}) = 2(\boldsymbol{n}_\alpha(\vec{r})\boldsymbol{n}_\beta(\vec{r}) - \frac{1}{2}\delta_{\alpha\beta})$, where $\mathbf{n}$ is a three-dimensional unit vector representing the orientation of a rod. At high temperatures, nematic textures contain both splay and bend deformations but upon lowering the temperature the texture becomes more splay- rich as shown in Figs. 2(c) and (d). These results demonstrate that lowering the temperature tunes up the elastic anisotropy of the nematic.

We further analyze these results by matching the texture near defect cores as described in the previous section. Figure 4 shows an example of the simulation con-

figuration and its matched asymptotic local texture, and Fig. 5(d) shows the calculated values of elastic anisotropy as a function of temperature. It is clearly seen that at high temperatures in the nematic phase, $\epsilon \approx 0$, i.e., $K_{11} \approx K_{33}$. Upon lowering the temperature, the elastic anisotropy gradually increases and the deformation is splay-dominated. We argue that these simulations are on the verge of the nematic to SmA transition, however, the process is never complete as indicated by the measured values of ϵ that are always less than 1.0. The argument is justified as the local orientation of the rods in the simulation follows the geodesic on the sphere as seen in Fig. 2(d).

We characterize the defect locations by matching four defects into two nearest-neighbor pairs, with each pair defining a great circle. The angle between the great circles is ϕ. In our simulations, the pairs are highly symmetrical so that the separation angle 2θ is similar for both pairs and we report only its average value. Finally, each defect director forms an angle γ with respect to its great circle. The angles for each of the defects are again always similar. Figures 5(a-c) shows θ, ϕ and γ as functions of temperature. We have, at higher temperatures, configurations close to tetrahedral arrangements, as expected from Refs. [1, 2, 4] at lower anisotropy values. In a perfect tetrahedral configuration, the angles must be $\theta = \frac{1}{2}\cos^{-1}(-1/3)$ and $\phi = \pi/2$, while γ is degenerate. It should be noted that at high temperatures, the anisotropy parameter is small but not identically zero in our simulations. This is the case for slightly deformed tetrahedral configurations, and indeed has been observed in most of the simulations around $\epsilon = 0$. Consequently, the value of θ shows large fluctuations. To get better statistics near the tetrahedral configuration, we average the angles over three possible great circle configurations.

Upon lowering the temperature, the anisotropy increases and the angles gradually decrease and we observe an incipient coalescence of the pairs, though this is never complete. At even lower temperatures, the positions of the defects move towards a great circle configuration where in the majority of our simulations they are approximately equally spaced $\theta = \pi/4$, $\phi = 0$, and the defect directors are anti-parallel and perpendicular to the common great circle $\gamma = \pi/2$. However, in limited simulations at very high densities, we observe a pair of defects moving towards the poles as shown in Fig. 1(c). The graph of the pair distance angle θ is non-monotonic as it decreases due to defect coalescence but increases again while approaching the great circle conformations. On the other hand, the angle between great circles ϕ has a smooth decreasing behavior.

We have also explored the effect of rod length and system size at various surface densities at $u/k_BT = 1.33$. We perform a large number of simulations by changing the rod length and surface density. Results for defect locations in these cases are summarized in Fig. 6, where the angles are plotted against the dimensionless ratio l/R. As with the case of temperature variations, changes in number density, length of the rod, and colloid size all modify the effective elastic constants. Here, the increments in density lead to stronger anisotropy in agreement with the previous report [25], and we again observe the flow from tetrahedral to coalescing to the great circle conformations. We note that trajectories depend on the specific realization of the nematic, though always follow the same general pattern.

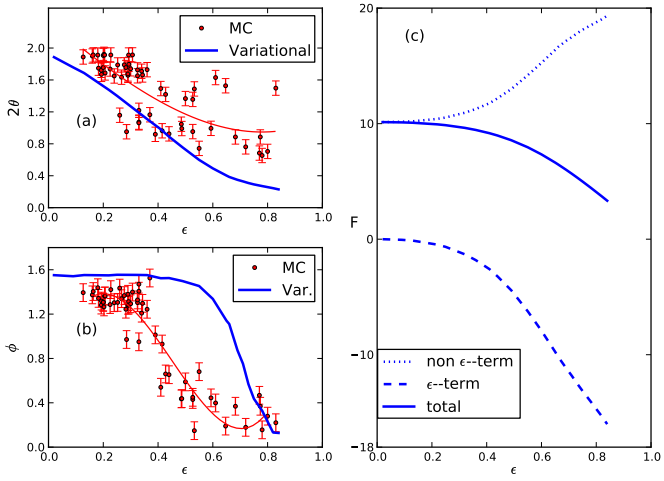

FIG. 7: (Color online) Comparison of simulation and variational results: (a) Polar angle (θ) as functions of ϵ. (b) Great circle angle (ϕ) as functions of ϵ. (c) Energy contribution from ϵ and non-ϵ term. The total energy is plotted as a solid line.

V. HARMONIC FIELD APPROXIMATION

As we have seen, the variation of several physical parameters induces a change in defect positions that can be consistently interpreted as a change in the effective elastic constants. For further insight into the change of defect positions with elastic constants we now turn to a variational approach [23]. We construct a set of analytically described textures and select among these the one with lowest free energy. If the texture space is large enough, the texture with minimum energy has properties similar to those of the true ground state of the Frank energy. We write F_o for this ground state energy and F_h for a generic harmonic texture. The minimum among the generic textures is F_{mh}. It is always true that the ground state is lower than or equal to this restricted minimum:

$$F_o \leq F_{mh} \leq F_h. \tag{4}$$

Our restriction to the space of harmonic textures has several advantages. It makes the minimization problem tractable in computational demands, it provides the possibility of heuristic insight, it allows us to use the defect positions as meaningful variables, it gives us upper bounds for the ground state, and it allows us to recover

the known exact result at the isotropic point $\epsilon = 0$. With these textures on hand it is also possible to consider generalizations of the method to non-harmonic configurations, though we will not consider these extensions in this article.

Here we use a modified version of the conformal mapping technique employed in Ref. [4] to create textures with prescribed defect locations. The sphere is mapped onto the complex plane by the standard holographic projection. In the complex plane, a potential $\Omega(z)$, analytical away from discrete singularities, is used to describe a planar texture. The angle of the nematic director α with respect to the real axis is obtained from the relation $\exp(-i\alpha) = \Omega'(z)/|\Omega'(z)|$. This director field is mapped back onto the sphere with the inverse holographic projection. Instead of presenting the potential, it is simplest to write down its derivative. We can show that the family of potentials with

$$\Omega'(z) = \frac{e^{i\delta}}{\sqrt{(z-z_1)(z-z_2)(z-z_3)(z-z_4)}} \qquad (5)$$

lead to well defined smooth nematic textures on the sphere with four 1/2 defects at locations that project onto the poles z_i. The phase factor $\exp(i\delta)$ adds an additional rotation of magnitude δ to the local field. This angle can be connected to the previously described γ angle describing the orientation of the defects. Connections between this and other texture descriptions are presented in the appendix. With these textures on hand, we can evaluate the Frank energy and determine, among them, the preferred location of the defects as a function of the anisotropy. Our explicit evaluations of the energy exclude a circle around defect cores of radius 0.02, for a unit sphere.

It has been shown before that in the absence of anisotropy, $\epsilon = 0$, the minimum energy corresponds to the tetrahedral arrangement of defects [1, 2, 4]. We find, in our variational approach, that the defect locations can always be organized into two pairs. As with our analysis of simulations, each pair defines a great circle. We arrange the intersections of the two circles to coincide with the north and south pole. One of the pairs is closer to the north pole and the second is near the south pole. In this construction, each of the defects is located at an angle θ from the respective pole. It turns out that the global rotation angle δ is always such that the directors of the defects are aligned with their great circle but point away from the pole. Thus, for each value of the anisotropy, the texture is easily described in terms of the cross angle ϕ and the polar displacement θ. This characteristic of the variational texture is clearly present in our simulations and justifies the use of the reduced set of parameters for the description of the defect conformations. The dependence of these angles on the anisotropy are presented in Fig. 7(a) and (b), where they are also contrasted with results from the simulations. While the variational approach selects configurations in which the nearest neighbors align their directors along the great circle, pointing towards the poles, we find in simulations that the nearest defect directors are also antiparallel but do not align with the great circle. It can be shown that that at $\epsilon = 0$ the energy is degenerate with respect to the global director rotations induced by the parameter δ, but at non-zero anisotropy the alignment with the great circles is always observed. On the other hand, it is also known that at $\epsilon = 1$, the true ground state consists of four $+1/2$ defects with arbitrary locations along a single great circle [5, 6]. Our approach can describe only one of those configurations, namely, one with coinciding locations for each of the pairs, i.e., they coalesce into two $+1$ defects. Thus, this method recovers the first process of coalescence but it is unable to fully reproduce the last process of alignment along the great circle. The nematic textures corresponding to the minimum free energy are plotted in Fig. 8. It clearly demonstrates the defect evolution presented above.

The variational calculation also offers further insight into the forces driving the defect flow. To get better insight into the driving forces between the defect interaction, we split the free energy into an ϵ-term and a non-ϵ-term. The numerical results are shown in Fig. 7(c). It is clear that a tetrahedral configuration arises from net repulsive interactions between the defects. Increasing the ϵ towards positive values simply increases the attraction between the pair of defects on the same hemisphere, and hence leads to the coalescing pair for $\epsilon = 1.0$. The overall evolution of the defect position with elastic anisotropy is illustrated in the animation the Supporting Information.

The variational approach we develop here has a number of limitations. First, we ignore the microscopic detail around a defect core which becomes important for a larger value of epsilon. Second, we assume that the defect structure can be always described with only three relevant variables, the angels (θ, ϕ, γ). This approximation breaks down when splay becomes highly dominant and the system texture presents four defects in a great circle and the positions of the defects can be arbitrary. This limitation is minor, however, as this occurs only in a very small range of the parameter space. On the other hand, we note that the variational method can be in principle extended to obtain more precise results that can match simulation and experimental observations. For this goal it would be necessary to modify the textures used. For example, it is possible to consider different functional forms for the behavior of the texture near the defect cores.

VI. CONCLUSION

In summary, we present a comprehensive description of the defect structure in spherical morphologies with surface crystalline order using two different approaches, Monte Carlo simulations and a variational calculation. The results show a continuous evolution of the defect structure from a tetrahedral configuration to pair coa-

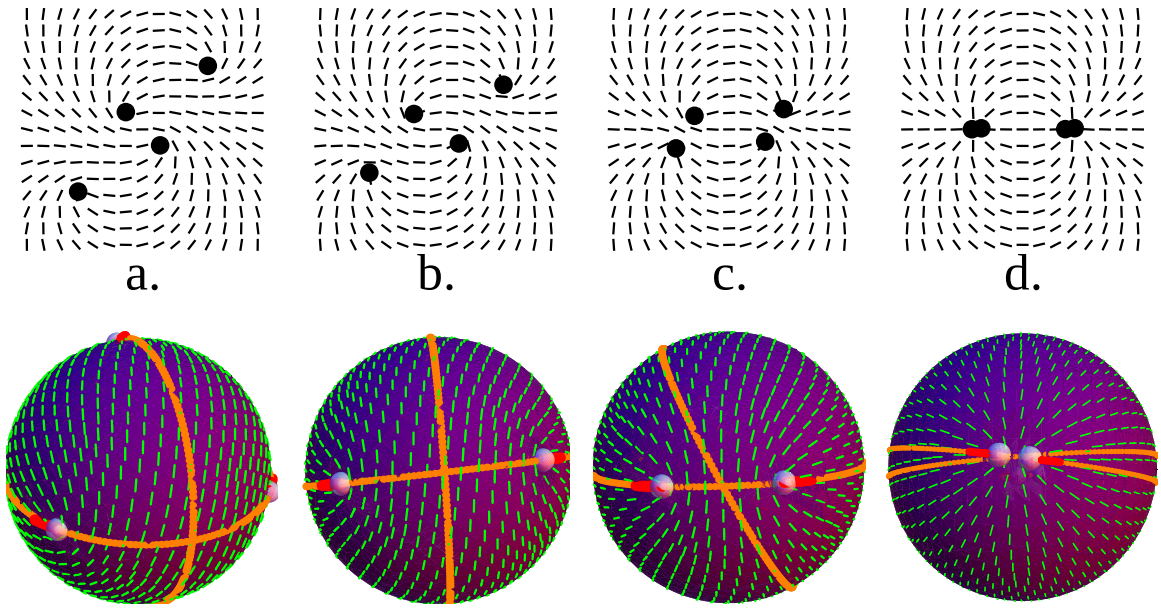

FIG. 8: (Color online) Harmonic nematic textures that minimize the free energy for different ϵ: (a) $\epsilon = 0.06$, (b) $\epsilon = 0.30$, (c) $\epsilon = 0.60$, and (d) $\epsilon = 0.90$. The top row shows their projection on the complex plane while the bottom row shows their realization in the sphere. The small spheres indicate the position of the defects, and their directors are marked as red rods.

lescence to a great circle arrangement upon increasing the ratio of splay to bend elastic constants of nematic. Our results clearly show how a perturbation in elastic constants can be realized by changing temperature, surface density, system size, and rod length. Our study of texture and defect structure in spherical nematics emphasizes their description by means of three angular parameters (θ, ϕ, γ). These parameters are sufficient to capture the defects arrangement. Additionally, we are able to directly map simulated textures to specific values of anisotropy by matching the known asymptotic shape of the textures to those that appear in the simulation. To complement this work, we show how textures described analytically can be used to approximate those observed in simulations. These analytic textures also permit the estimation of energies in the system, and can in principle be further refined for better agreement. In addition to providing a fuller picture of a very geometry-rich system, the techniques we develop here can be valuable in the study of defect structures in other geometries, for example, on elliptical surfaces. The analytical approach developed here can also be useful in the study of dynamical processes involving textures in diverse geometries such as the faceted tetrahedra induced by the defects in the tetrahedral configuration in deformable membranes with surface liquid crystalline order [26].

Acknowledgments

We would like to thank Chloe Funkhouser for a critical reading of the manuscript. Computational resources were provided by the Quest cluster at Northwestern University. We acknowledge the support of the NERC, which is an EFRC funded by the DOE Office of Science under Award DE-SC0000989.

Appendix A: Harmonic field and nematic texture

In this Appendix, we provide the details for various useful representations of the nematic textures and their energies. We consider two-dimensional vector representations of the nematic field and demonstrate the construction of families of textures using complex fields. The energy of the textures is written in the form of squares of curvatures as well as in terms of the complex derivatives of an angle variable.

Locally, a nematic texture can be described by a normalized three-dimensional vector field $\mathbf{n}$, with $\mathbf{n}\cdot\mathbf{n} = 1$. Globally, this field has discontinuities at defect sites and at seams where the vector inverts its direction. It is useful to introduce a conjugate field $\mathbf{m}$, obtained by rotating the field $\mathbf{n}$ by an angle $\pi/2$ at each point about the corresponding normal. As the nematic molecules are confined on the spherical surface with a strong tangential anchoring, we can introduce a two-dimensional representation for them. In a two-dimensional representation, the vector $\mathbf{n}$ is described by two components n^i, $i = 1, 2$. If

the surface is parametrized by the coordinates x^i, we can define a set of basis vectors as $\mathbf{e}_i = \partial\mathbf{X}/\partial x^i$, where $\mathbf{X}$ is the three-dimensional position vector on the surface of a sphere. With these definitions, the metric of the surface is defined as $g_{ij} = \mathbf{e}_i \cdot \mathbf{e}_j$. Associated with this metric, we have a covariant derivative ∇_i that projects the usual gradient in three-dimensional space onto the surface. This covariant derivative is the same as the one used in writing the Frank free energy in Eq. (1), but here we wish to stress its intrinsic form as an operator in a two-dimensional manifold. The components of the covariant derivative of a vector field are defined as: $\nabla_i v^j = \partial_i v^j + \Gamma^j_{ik} v^k$,where Γ^j_{ik} are the Christoffel symbols for the metric.

We now proceed to write the nematic free energy using the two-dimensional representation of the nematic field. As noted, for example, in Ref. [2], the two components of the Frank free energy can be described by terms quadratic on the curvatures of the field lines and equipotential curves associated with a texture. We first construct these two curvatures, κ_b and κ_s in terms of the vector field $\mathbf{n}$. If we follow the field $\mathbf{n}$ along the streamlines it defines, we can find its rate of change, tangent to surface, as $n^i\nabla_i n^j$. This vector must have the same direction as the conjugate field m^i since $n^i n_i = 1$ and $n^k\nabla_k(n^i n_i) = 2n^i n^k \nabla_k n_i = 0$. Thus, the magnitude of the derivative gives us the curvature of the streamlines along the surface $\kappa_b = \pm m_j(n^i\nabla_i n^j)$. Since, $n^i m_i = 0$, we can write $\kappa_b = \mp n^i(n^j\nabla_j m_i)$.

Since the derivative of m^i has no component along m^i itself, we can add a null term to the curvature expression and write $\kappa_b = \mp(n^i n^j + m^i m^j)\nabla_j m_i$. We note that we have the equality $g^{ij} = n^i n^j + m^i m^j$, which can be checked by direct evaluation in a given set of coordinates. For example, at a point where coordinates are orthonormal, it is easy to check that both tensors are equal to the identity matrix, and are therefore equal in any other system of coordinates. This observation reduces our expression to $\kappa_b = \mp\nabla_i m^i$. The respective term in the Frank free energy is proportional to the square of this curvature, i.e.,

$$\frac{1}{2}K_{33}\kappa_b^2 = \frac{1}{2}K_{33}(\nabla_i m^i)^2. \tag{A1}$$

To obtain the second curvature, we note that the splay of a vector field is associated with distortions of the field n^i as we travel along the transverse direction m^i. That is, we should evaluate the directional derivative $m^k\nabla_k n^i$. This expression has also an interpretation as the curvature κ_s of the streamlines of the field m^i. As in the previous case, we contract with the transversal direction to obtain its magnitude $\kappa_s = \pm m_i m^k \nabla_k n^i$ and after adding null terms proportional to $n^i n^j$ we obtain $\kappa_s = \pm\nabla^i n^i$. Hence, we can write

$$\frac{1}{2}K_{11}\kappa_s^2 = \frac{1}{2}K_{11}(\nabla_i n^i)^2. \tag{A2}$$

The total free energy has therefore the alternative representation

$$F = \int d^2x\sqrt{g}\frac{1}{2}\left[K_{11}(\nabla_i n^i)^2 + K_{33}(\nabla_i m^i)^2\right]. \tag{A3}$$

Next, we connect this representation of the energy with a description of the field by means of a complex potential. As the sphere is two-dimensional, it is possible to use a single complex coordinate z to label its points, at least locally. The complex representation we will use, the holographic projection, has some unique properties, such as being conformal with respect to the metric of the sphere. Conformal metrics take the form $g_{ij}dx^i dx^j = f(z,\bar{z})dzd\bar{z}$ in complex coordinates. The holographic projection maps a point in the unit sphere to the intersection between the plane tangent to the south pole and a chord passing through the north pole and the given point. A point on the sphere with coordinates (θ,ϕ) is then mapped to the complex plane position $z = 2\cot(\theta/2)e^{i\phi}$. The coordinate z and its conjugate $\bar{z}$ define a basis $\mathbf{e}_z = \partial_z\mathbf{X}$, $\mathbf{e}_{\bar{z}} = \partial_{\bar{z}}\mathbf{X}$. A vector expressed in this basis is real if its components are related as $v^z = \overline{v^{\bar{z}}}$. When using these coordinates, we replace the tensor indices $i = 1,2$ with $i = z,\bar{z}$. In these coordinates the metric of the sphere is

$$g_{ij} = \frac{8}{(4+z\bar{z})}\begin{pmatrix} 1 & 0 \\ 0 & 1 \end{pmatrix}. \tag{A4}$$

Using this metric, we obtain the Christoffel symbols needed for the covariant derivative. We have:

$$\Gamma^z_{zz} = -\frac{1}{2}\frac{\bar{z}}{(4+z\bar{z})}. \tag{A5}$$

and $\Gamma^{\bar{z}}_{\bar{z}\bar{z}} = \overline{\Gamma^z_{zz}}$. The symbols are equal to zero for all other combination of indices.

In the main text of this article, we have presented the nematic field in terms of an angle α with respect to the x- axis of the holographic projection as $\exp(-i\alpha) = \Omega'(z)/|\Omega'(z)|$. We can construct an explicit representation of the vector as follows. We note that, in the holographic projection plane, the vector field $(N^x, N^y) = (\cos(\alpha), \sin(\alpha))$ has the correct direction but is not normalized. Using the complex variables $(z,\bar{z})$ in this plane, the vector has a representation proportional to $(\exp(i\alpha), \exp(-i\alpha))$, which has a norm $\sqrt{2g_{z\bar{z}}}$. We can then write

$$n^i = \frac{1}{\sqrt{2g_{z\bar{z}}}}(\exp(i\alpha), \exp(-i\alpha)) \tag{A6}$$

$$= \frac{1}{\sqrt{2g_{z\bar{z}}}}\left(\sqrt{\frac{\overline{\Omega'(z)}}{\Omega'(z)}}, \sqrt{\frac{\Omega'(z)}{\overline{\Omega'(z)}}}\right). \tag{A7}$$

The conjugate field is

$$m^i = \frac{1}{\sqrt{2g_{z\bar{z}}}}(i\exp(i\alpha), -i\exp(-i\alpha)) \tag{A8}$$

$$= \frac{1}{\sqrt{2g_{z\bar{z}}}}\left(i\sqrt{\frac{\overline{\Omega'(z)}}{\Omega'(z)}}, -i\sqrt{\frac{\Omega'(z)}{\overline{\Omega'(z)}}}\right). \tag{A9}$$

The covariant derivatives of these fields involve three types of terms, a partial derivative of the angle, $\partial_z\alpha$ or $\partial_{\bar{z}}\alpha$, the Christoffel term proportional to Γ^z_{zz} or its conjugate, and the derivative of the normalizing factor, $\partial_z(2g_{z\bar{z}})^{-1/2}$ or its conjugate. The last derivative, however, is proportional to the Christoffel symbol, and it is then possible to write the components of the covariant derivatives as

$$\nabla_z n^z = \frac{1}{\sqrt{2g_{z\bar{z}}}}\exp(i\alpha)(\partial_z\alpha + H_z) \quad \text{(A10)}$$

$$\nabla_{\bar{z}} n^{\bar{z}} = \frac{1}{\sqrt{2g_{z\bar{z}}}}\exp(-i\alpha)(\partial_z\alpha + H_{\bar{z}}), \quad \text{(A11)}$$

where the effective connection terms H_z are equal to half the corresponding Christoffel symbols, $H_z = (1/2)\Gamma^z_{zz}$.

In the main text we introduced a potential of the form

$$\Omega'(z) = \frac{e^{i\delta}}{\sqrt{(z-z_1)(z-z_2)(z-z_3)(z-z_4)}}. \quad \text{(A12)}$$

This potential differs from the one used in Ref. [2]. Their selection adds a factor so as to have an angle measured from the meridians of the sphere while the angle we use is measured with respect to the x-axis in the plane. In the format we offer, the positions of the defects are more clearly identified.

The free energy of the texture can be evaluated using known expressions in terms of the local angle or by using the constructions presented above. It is useful to split the free energy into two contributions, one independent of ϵ, and one linear in this parameter. We first write

$$f = \frac{1}{2}K_{33}(\nabla_i n^i)^2 + \frac{1}{2}K_{11}(\nabla_i m^i)^2 \quad \text{(A13)}$$

$$= \frac{1}{2}K_{33}(\nabla_z n^z + \nabla_{\bar{z}} n^{\bar{z}})^2 - \frac{1}{2}K_{11}(\nabla_z n^z - \nabla_{\bar{z}} n^{\bar{z}})^2. \quad \text{(A14)}$$

We split the terms in the last expression, using coefficients f_ϵ and f_h for the terms dependent and independent of ϵ, respectively. We can evaluate them, for example, in terms of the angle α

$$f = (K_{11}+K_{33})\left[f_h + \epsilon f_\epsilon\right], \quad \text{(A15)}$$

$$f_h = (\partial_z\alpha\partial_{\bar{z}}\alpha + H_{\bar{z}}\partial_z\alpha + H_z\partial_{\bar{z}}\alpha + H_{\bar{z}}H_z), \quad \text{(A16)}$$

$$f_\epsilon = Re\left[e^{2i\alpha}(\partial_z\alpha + H_z)^2\right], \quad \text{(A17)}$$

where the operator $Re[]$ extracts the real part of the expression.

[1] T. C. Lubensky and J. Prost., J. Phys. II (France) **2**, 371 (1992).
[2] D. R. Nelson, Nano Lett. **2**, 1125 (2002).
[3] G. A. DeVries *et al.*, Science **315**, 358 (2007).
[4] V. Vitelli and D. R. Nelson, Phys. Rev. E **74**, 021711 (2006).
[5] M. A. Bates, J. Chem. Phys. **128**, 104707 (2008).
[6] H. Shin, M. J. Bowick, and X. Xing, Phys. Rev. Lett. **101**, 037802 (2008).
[7] G. Skacej and C. Zannoni, Phys. Rev. Lett. **100**, 197802 (2008).
[8] S. Kralj, R. Rosso, and E. G. Virga, Soft Matter **7**, 670 (2011).
[9] R. L. B. Selinger, A. Konya, A. Travesset, and J. V. Selinger, J. Phys. Chem. B **115**, 13989 (2011).
[10] J. Dzubiella, M. Schmidt, and H. Lwen, Phys. Rev. E **62**, 5081 (2000).
[11] A. C. Callan-Jones, R. A. Pelcovits, V. A. Slavin, S. Zhang, D. H. Laidlaw, and G. B. Loriot, Phys. Rev. E **74**, 061701 (2006).
[12] B. L. Mbanga, G. M. Grason, and C. D. Santangelo, Phys. Rev. Lett. **108**, 017801 (2012).
[13] W. Y. Zhang, Y. C. Jiang,and Z. Y. Jeff, Phys. Rev. Lett. **108**, 057801 (2012).
[14] T. Lopez-Leon *et al.*, Nature Phys. **7**, 391 (2011).
[15] T. Lopez-Leon, A. Fernandez-Nieves, M. Nobili, and C. Blanc, Phys. Rev. Lett. **106**, 247802 (2011).
[16] H. L. Liang, S. Schymura, P. Rudquist, and J. Lagerwall, Phys. Rev. Lett. **106**, 247801 (2011).
[17] A. Fernandez-Nieves *et al.*, Phys. Rev. Lett. **99**, 157801 (2007).
[18] M. A. Horsch, Z. L. Zhang, and S. C. Glotzer, J. Chem. Phys. **125**, 184903 (2006).
[19] A. Dewar and P. J. Camp, Phys. Rev. E **70**, 011704 (2004)
[20] J. Xu, R. L. B. Selinger, J. V. Selinger, B. R. Ratna, and R. Shashidhar, Phys. Rev. E **60**, 5584 (1999).
[21] J. D. Weeks, D. Chandler, and H. C. Andersen, J. Chem. Phys.**54**, 5237 1971; D. Chandler, J. D. Weeks, and H. C. Andersen, Science **220**, 787 (1983).
[22] D. Frenkel and B. Smit, *Understanding Molecular Simulation: From Algorithms to Applications* (Academic, New York, 2002).
[23] G.S. Ranganath, Mol. Cryst. Liq. Cryst. **97**, 77 (1983).
[24] I. E. Dzytaloshinskii, Zh. Eksp. Teor. Fiz. **58**, 1443 (1970) [Sov. Phys. JETP **31**, 773 (1970)].
[25] S.-D. Lee and R. B. Meyer, Phys. Rev. Lett. **61**, 2217 (1988).
[26] X. Xing ,H. Shin, M.J. Bowick , Z. Yao ,L. Jia, and M. H. Li, PNAS, **109**, 5202-6 (2012).